Press-compaction-assisted Binder Jetting of Textured Ceramics

Mohammadamin Moghadasi[a], Alireza Mahdaviarab[b], Anna-Katharina Hofer[c], Raul Bermejo[c], Zhijian Pei[d], Chao Ma[a,d,e,f*]

[a] Department of Materials Science and Engineering, Texas A&M University, College Station, TX, USA

[b] Department of Computer Science and Engineering, Texas A&M University, College Station, TX, USA

[c] Department of Materials Science, Montanuniversität Leoben, Leoben, Austria

[d] Department of Industrial and Systems Engineering, Texas A&M University, College Station, TX, USA

[e] Department of Engineering Technology and Industrial Distribution, Texas A&M University, College Station, TX, USA

[f] School of Manufacturing Systems and Networks, Arizona State University, Mesa, AZ, USA

*Corresponding author. E-mail address: chao_ma@asu.edu (Chao Ma)

Abstract

In this work, textured ceramics were successfully obtained using press-compaction-assisted binder jetting for the first time. A mixture of alumina nanoplatelets and nanoparticles was used as the feedstock powder (the nanoplatelets served as templates for epitaxial grain growth during sintering while the nanoparticles were consumed by the grain growth). The nanoplatelet fraction in the mixture was varied from 0 wt.% to 50 wt.%. Green samples were prepared with a lab-designed press-compaction-assisted binder jetting machine. The green samples were then sintered in a furnace and their sintered densities were measured. A scanning electron microscope and X-ray diffractometer were used to investigate the degree of texture in the sintered samples. Finally, the biaxial flexural strength of the sintered samples was measured. As the nanoplatelet fraction increased, the sintered density decreased, but the degree of texture increased. Interestingly, the biaxial flexural strength of the sintered samples with 5 wt.% or 10 wt.% nanoplatelets was higher than those without nanoplatelets, suggesting the increased degree of texture has a stronger effect on the mechanical response than the reduced sintered density under these conditions.

Keywords

Binder jetting, Additive manufacturing, Textured ceramics, Templated grain growth

1 Introduction

The crystal structure of numerous ceramic materials is anisotropic. As a result, their thermo-elastic properties may differ in different directions. However, due to the random orientation of the grains, the property differences along different directions are balanced out, thus providing polycrystalline ceramics with an isotropic behavior [1]. By texturing ceramics, it is possible to take advantage of grains' anisotropic nature and improve their performance. Through texturing, the grains get preferentially aligned, and therefore, the desired properties of ceramics could be tailored along specific directions. This allows for an expansion of the ceramics' potential applications, as their tailored properties open up new possibilities for their use [2,3]. For instance, it was previously demonstrated that by achieving the lamellar textured structure and the alignment of elongated grains, the fracture toughness and strength of ceramics were improved in the direction perpendicular to the grain alignment [4–6].

Templated grain growth (TGG) is among the most widely used methods for texturing ceramics [7–10]. TGG can be divided into three steps: 1) adding templates (e.g., nanoplatelets) to the matrix powder (e.g., nanoparticles); 2) aligning the added templates along the preferred orientation by mechanical, magnetic, or other means; 3) epitaxially growing the preferentially aligned templates at the expense of matrix powder at a high temperature.

Although textured ceramics can be successfully fabricated with the TGG method, the manufacturing of complex-shaped textured ceramics is challenging [2]. Recently, some studies have been reported on texturing ceramics using additive manufacturing processes, such as material extrusion and vat photopolymerization [11–13]. However, to the best of the authors' knowledge, no research has been done on the possibility of producing textured ceramics using binder jetting. The advantages of binder jetting over other additive manufacturing processes include the complimentary support for overhang structures and ease of debinding [14–18].

In this work, binder jetting was attempted to fabricate textured ceramics for the first time. A mixture of alumina nanoplatelets and nanoparticles was used as the feedstock powder. The nanoplatelets served as the templates while the nanoparticles served as the matrix powder. The nanoplatelet fraction in the feedstock powder was varied from 0 wt.% to 50 wt.%. Green density, sintered density, and sintering shrinkage were measured. The microstructure was analyzed using

scanning electron microscopy (SEM) and X-ray diffraction (XRD). Biaxial flexural strength was measured and evaluated according to Weibull statistics.

2 Materials and Methods

2.1 Feedstock powder

De-agglomerated alumina nanoparticles (90–187125, Allied High Tech, USA) were employed as the matrix powder. Alumina nanoplatelets (1344-28-1, Antaria Pty Ltd, Australia) of were added as the templates to the alumina nanoparticles. The nanoplatelet fraction in the mixture was varied from 0 wt.% to 50 wt.%. Following the ASTM standard [19], the apparent densities of alumina nanoparticles and nanoplatelets were measured to be 6.4 % and 5.8 %, respectively. Figures 1a and 1b show the morphology of the alumina nanoparticles and nanoplatelets, respectively. Calcium carbonate ($CaCO_3$) powder (US3701, US Research Nanomaterials, USA) with a particle size of smaller than 50 nm, and silicon dioxide (SiO_2) powder (US1161M, US Research Nanomaterials, USA) with a particle size of 200 nm, were used as sintering aids. The final powder mixture consisted of 5 wt.%. sintering aids (calcium carbonate and silicon dioxide with a molar ratio of 1:1) and 95 wt.% alumina powders (nanoplatelets and nanoparticles). The powder mixture was ball milled (Jar Rolling Mills, Paul O. Abbe, USA) for 1 h using alumina balls with a diameter of 6 mm. The weight of alumina balls was the same as the weight of the powder mixture. The milling speed was 160 RPM. After ball milling, the powder mixture was sieved with an opening size 250 μm.

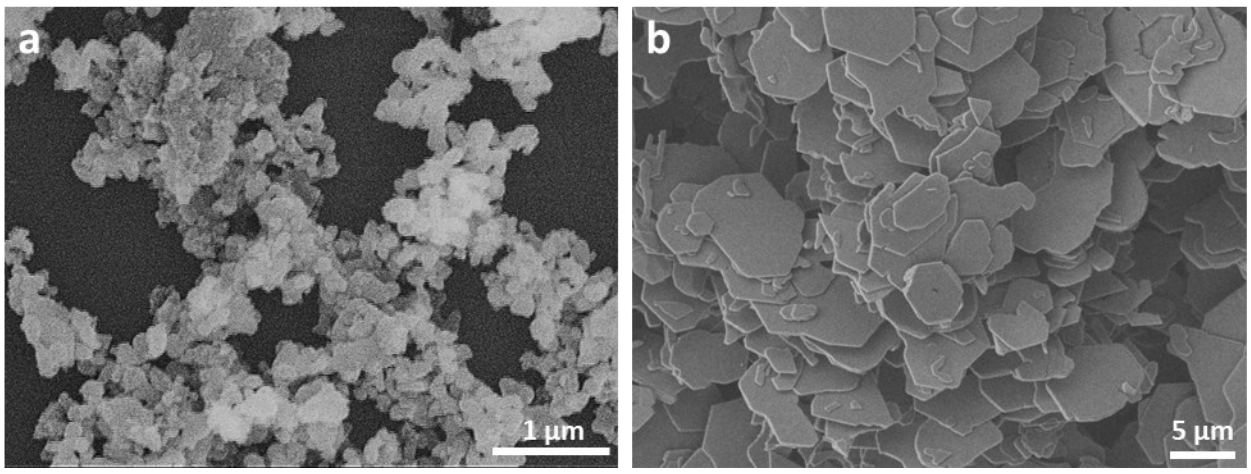

Figure 1. SEM images of a) alumina nanoparticles (matrix powder) b) alumina nanoplatelets (templates).

2.2 Press-compaction-assisted binder jetting

A lab-designed press-compaction-assisted binder jetting machine was used to fabricate green samples. The press-compaction-assisted binder jetting process is derived from a recently issued patent [20] from Tethon 3D (a company specialized in additive manufacturing machines and feedstock materials). The schematic of the sample preparation steps is shown in Figure 2. In Step 1, the build plate was lowered by the height of one layer thickness (LT) plus the compaction thickness (CT). In Step 2, the feedstock powder was spread using a metal blade to fill the gap over the build plate. In Step 3, by covering the top of the powder bed with a cap and raising the build plate by the height of CT, the spread powder was compacted. Thus, in this way, the new compacted layer was made with the height of LT. This printing process was repeated for each layer until the entire sample was prepared. In this research, LT and CT were fixed at 50 µm and 450 µm, respectively. The sample height and diameter were fixed at 2 mm and 19 mm, respectively.

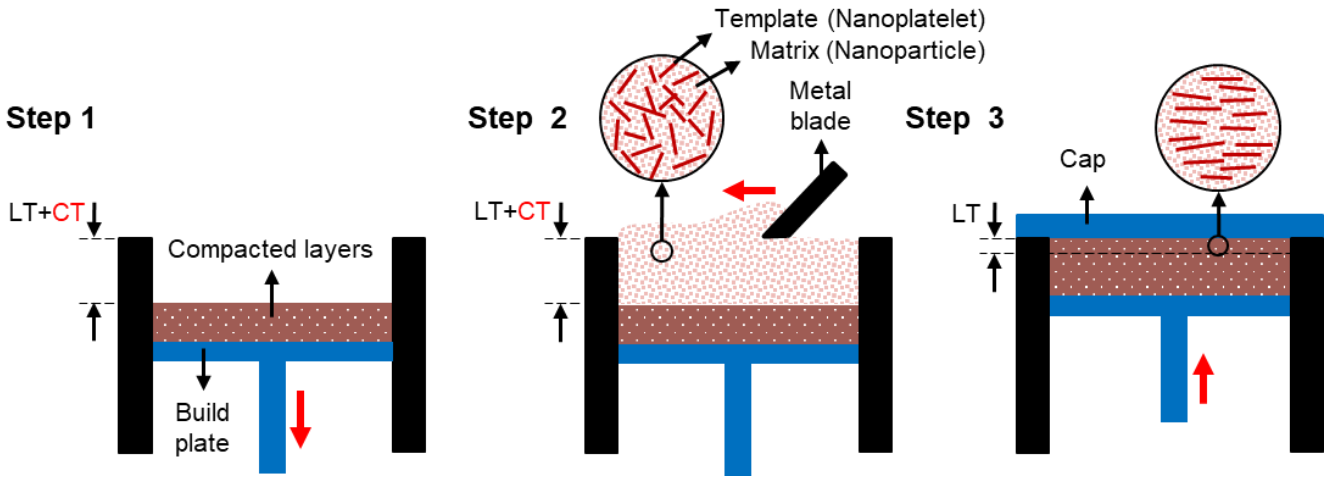

Figure 2. Steps of the press-compaction-assisted binder jetting process (LT and CT mean layer thickness and compaction thickness, respectively).

2.3 Calcination and sintering processes

The green samples were placed in a furnace (KSL-1700X-A1-UL, MTI Corp., USA) for calcination and sintering. The heating profile plotted in Figure 3 was implemented. For calcination, the furnace was heated up from room temperature to 800 °C with a heating rate of 5 °C/min and kept at 800 °C for 1 h. For full sintering, the temperature was increased to 1100 °C with 5 °C/min and then to 1700 °C with 2 °C/min and kept at 1700 °C for 2 h. For partial sintering, the final

temperature was increased to 1500 ºC instead of 1700 ºC. Finally, the furnace was turned off, and the samples were left in the furnace for cooling.

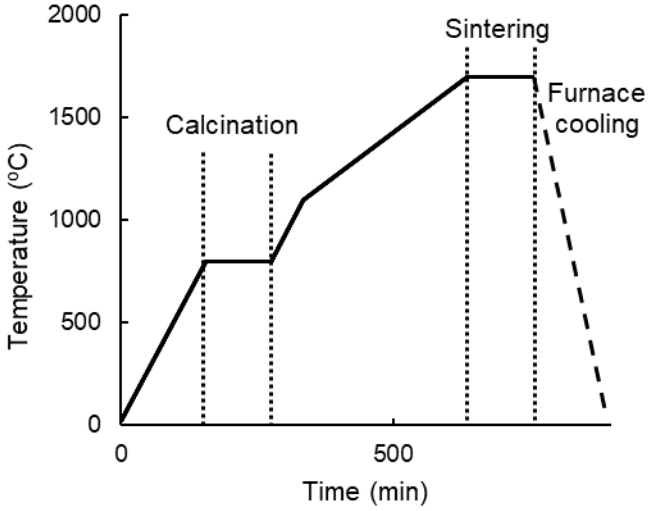

Figure 3. Temperature profile used for calcination and sintering.

2.4 Green density, sintered density, and sintering shrinkage measurements

The density of the green samples was determined by measuring their weight, diameter, and thickness. The density of the sintered samples was obtained following the Archimedes' method [21]. For the sintering shrinkage, the diameters of the samples before and after sintering were measured. The density and shrinkage measurements were conducted on at least five samples for each condition.

2.5 Characterization of microstructure

SEM and XRD were used to study the morphological and crystallographic texture, respectively. For morphological texture investigation through SEM (FERA-3, TESCAN, Czech Republic), high-magnification images were taken from the cross-sections of the samples to examine the orientation of the nanoplatelets. For crystallographic texture assessment, XRD (D8 X-ray, BRUKER, USA) tests were conducted on the top surfaces and side cross-sections of the samples. Additionally, XRD tests were carried out on the top surfaces of the samples before and after sintering to investigate the effect of TGG.

2.6 Mechanical testing

Biaxial flexural tests were used to investigate the effect of texturing on the mechanical behavior of the sintered samples. The ASTM standard was followed [22]. The tests were conducted on the three series of samples: with 0 wt.%, 5 wt.% and 10 wt.% nanoplatelets. For statistical significance of the results, 10 samples of each series, in total 30 samples, were tested. In this measurement, the samples were placed in the center of the test fixture with three supports at the bottom which were positioned 120° apart on a circle of 10 mm in diameter. The loading plunger came from the top of the samples. The load was applied to the center of the samples until they fractured. The load and displacement of the loading plunger were recorded. The biaxial flexural strength was calculated.

3 Results and discussion

3.1 Green density, sintered density, and sintering shrinkage

Figure 4 shows the relationship between nanoplatelet fraction and green density. These results indicate that regardless of the nanoplatelet fraction, the average green density does not considerably change, likely due to the strong press compaction during the sample preparation process.

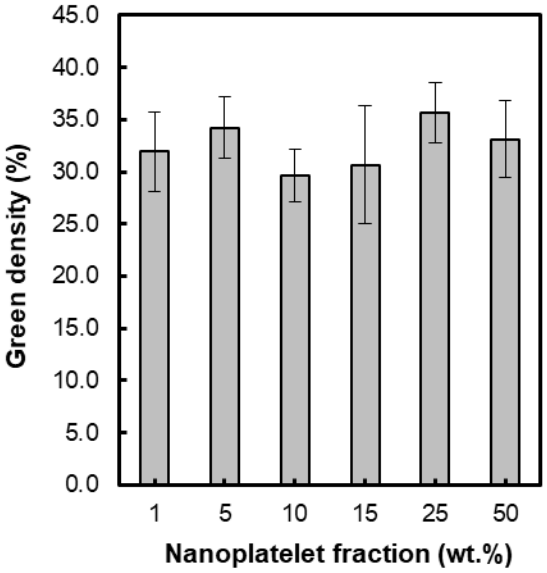

Figure 4. Relationship between nanoplatelet fraction and green density.

Unlike the green density, the sintered density and sintering shrinkage results show that they are significantly affected by nanoplatelet fraction, as shown in Figure 5. As nanoplatelet fraction increases (in other words, as the nanoparticle fraction decreases), the sintered density and sintering shrinkage decrease. These declining trends may be attributed to template impingement. The growth of templates in preferred direction reduces their ability to rearrange and causes interference among them, which limits growth and reduces the ability of pore closure [9,23]. Large nanoplatelet fractions have been shown to reach the state of template impingement earlier as than small fractions [9]. These declining trends may also correlate with the available fraction of matrix powder. TGG is based on coalescence, where the surrounding nanoparticles are consumed by templates [2]. With increasing the nanoplatelet fraction, there are fewer nanoparticles as the matrix powder available to be consumed by templates for their growth.

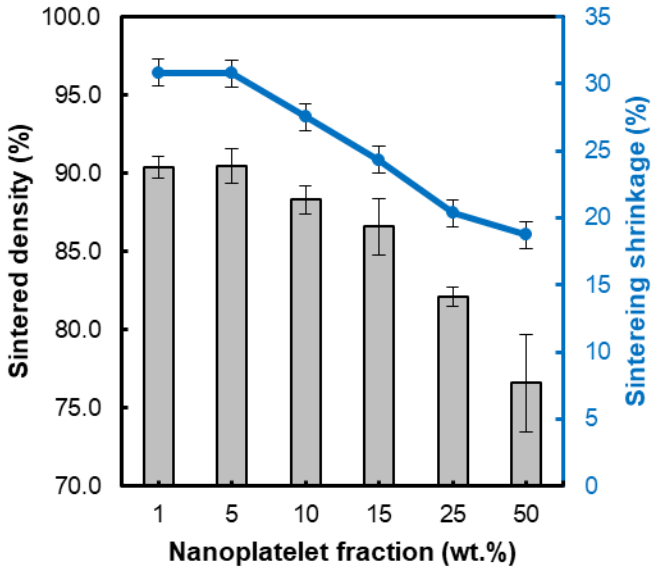

Figure 5. Effects of nanoplatelet fraction on sintered density and sintering shrinkage.

3.2 Scanning electron microscopy analysis

To assess the alignment of the nanoplatelets, SEM images were taken from the partially sintered samples, as shown in Figure 6. The images were taken from the cross-sections of the samples that were parallel to the build direction. Figure 6 demonstrates that most of the nanoplatelets are oriented horizontally and aligned perpendicularly to the build direction (yellow

arrow in Figure 6b). This alignment of the nanoplatelets could be attributed to spreading and compacting the powder layer by layer during the press-compaction assisted binder jetting process.

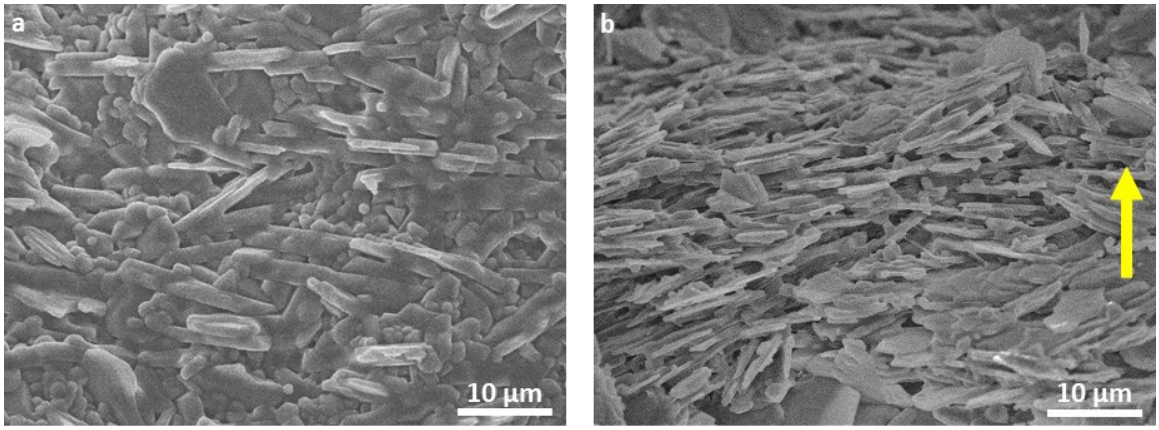

Figure 6. SEM images of partially sintered samples with a) 10 wt.% and b) 50 wt.% nanoplatelets (the build direction is shown with the yellow arrow)

In addition to the SEM images of partially sintered samples, SEM images were taken from the cross-sections of the fully sintered samples with various nanoplatelet fractions. Figure 7a shows that, without nanoplatelets, an equiaxed structure was formed without preferred orientations. However, by adding nanoplatelets and increasing their fraction, the structure became textured, as shown in Figures 7b through 7d. As in the case of partially sintered samples, most of the templated grains are horizontally oriented.

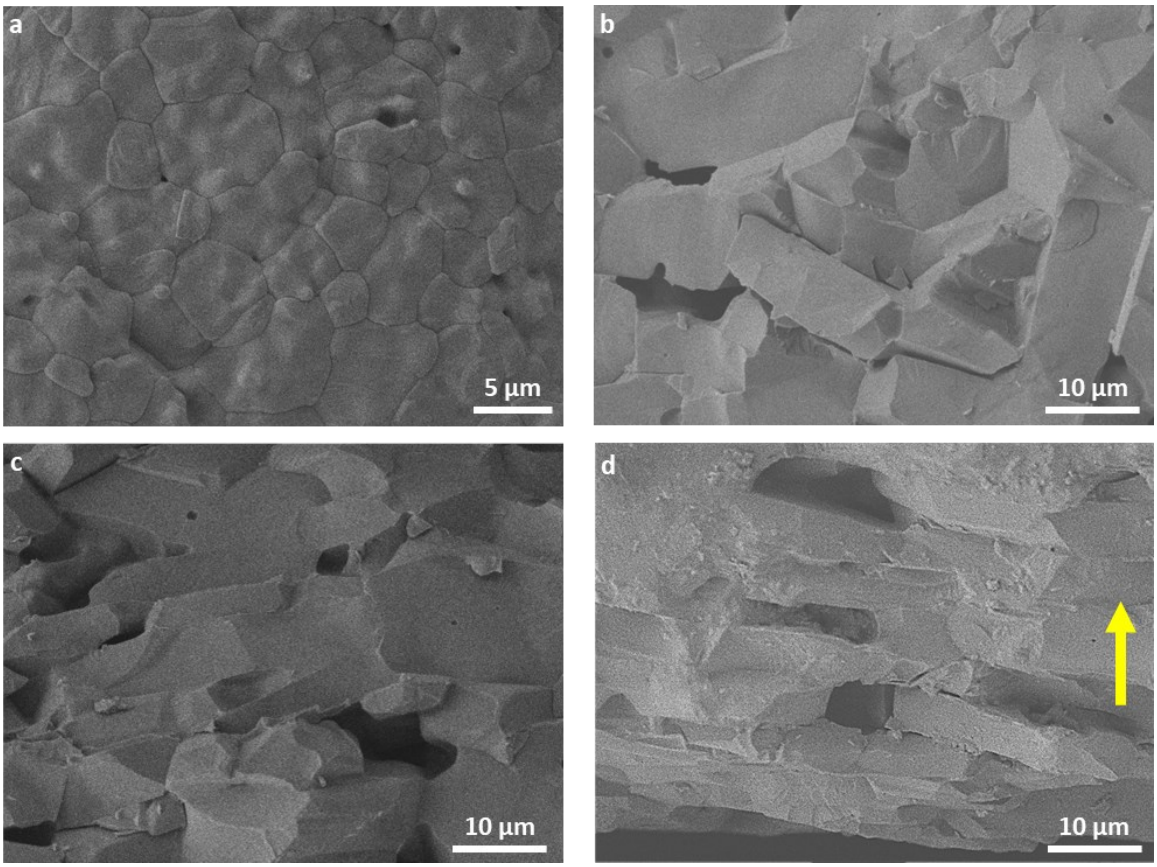

Figure 7. SEM images of fully sintered samples a) without nanoplatelets, b) with 5 wt.% nanoplatelets, c) with 10 wt.% nanoplatelets, and d) with 50 wt.% nanoplatelets (the build direction is shown with the yellow arrow)

3.3 X-ray diffraction analysis

3.3.1 Evidence of textured structure

Figure 8 demonstrates the XRD patterns of the top surface of the fully sintered sample without nanoplatelets (Figure 8a), as a reference, compared with the top surface and side cross-section of the fully sintered sample with 50 wt.% nanoplatelets (Figures 8b and 8c). It is clear that these three XRD patterns are different from each other.

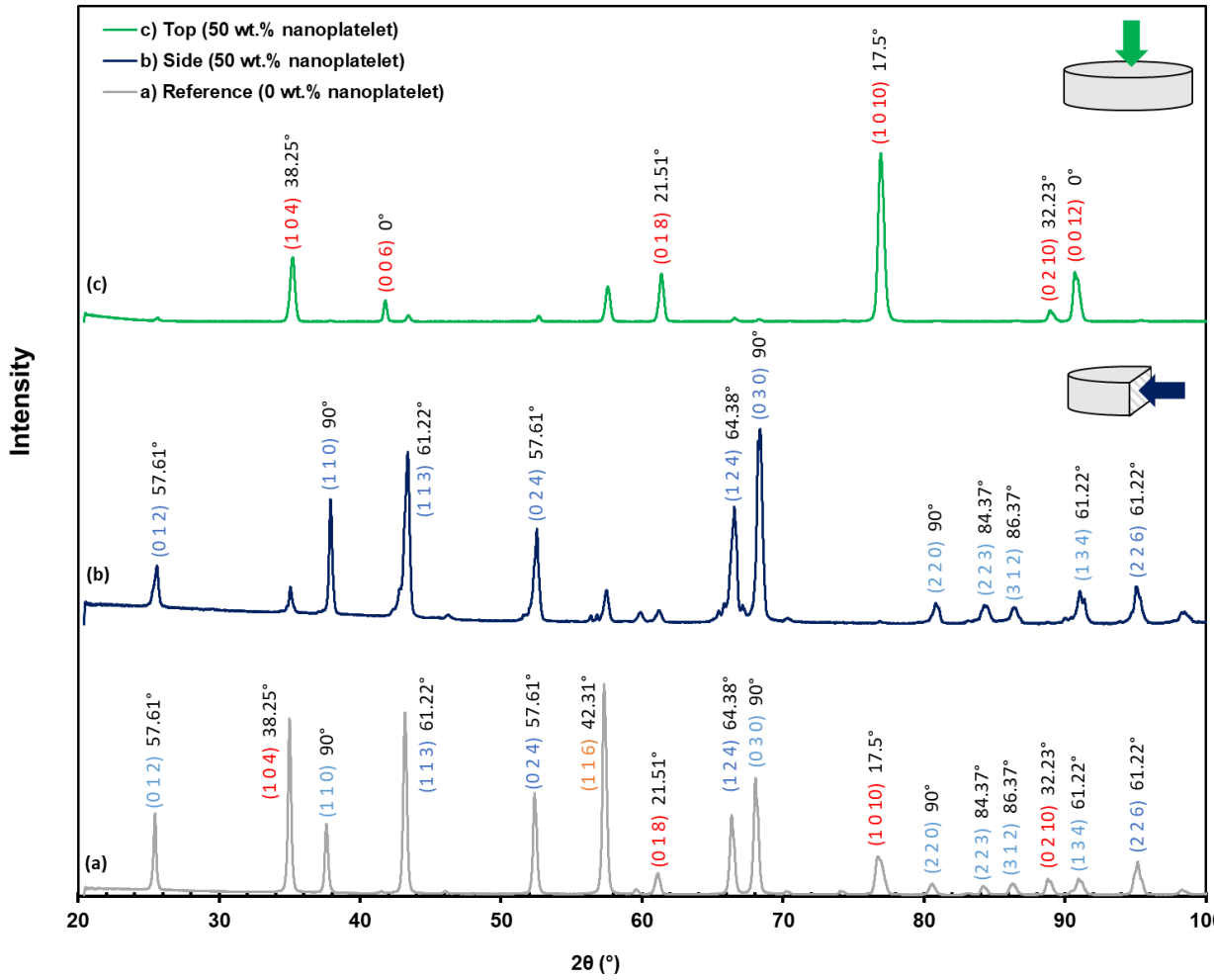

Figure 8. XRD patterns of a) the top surface of the sintered sample without nanoplatelets, b) the side cross-section of the sintered sample with 50 wt.% nanoplatelets, and c) the top surface of the sintered sample with 50 wt.% nanoplatelets.

To explain how the different XRD patterns could be related to the textured structure, the interplanar angle between the diffracted plane (h k l) and the basal crystal plane (0 0 6) of the hexagonal unit cell of α-alumina was calculated using the following equation:

$$\cos \emptyset_{hkl} = \frac{\frac{\sqrt{3}a}{2c} l}{\sqrt{h^2 + k^2 + hk + \frac{3a^2}{4c^2} l^2}} \qquad (1)$$

where a and c are the lattice parameters of the α-alumina unit cell and are equal to 4.758 Å and 12.991 Å, respectively. In this paper, interplanar angle always refers to the angle between a plane

of interest (h k l) and the basal crystal plane (0 0 6). Table A1 shows the calculated interplanar angles for the main characteristic diffracted planes of α-alumina. The diffracted planes were divided into three groups with small ($\emptyset_{hkl} < 40°$), medium ($40° < \emptyset_{hkl} < 50°$), and large ($\emptyset_{hkl} > 50°$) interplanar angles, respectively. These groups are specified in Table A1 and highlighted with symbols of different colors in Figure 8 (small = red, medium = orange, and large = blue).

The XRD pattern of the reference sample, i.e., without nanoplatelets, consists of a wide range of interplanar angles from small to large, as shown in Figure 8a. The high-intensity peaks of (1 0 4), (1 1 6), and (1 1 3) in Figure 8a, which are recognized as the typical peaks of α-alumina [24,25], have small (38.25°), medium (42.31°), and large (61.22°) interplanar angles, respectively.

The sintered sample with 50 wt.% nanoplatelets shows completely different XRD patterns from the reference sample. The XRD pattern of the side cross-section of the sintered sample with 50 wt.% nanoplatelets, Figure 8b, is dominated by the peaks with large interplanar angles. The high-intensity peaks of the side cross-section include (0 3 0), (1 1 3), and (1 1 0) and have large interplanar angles of 90°, 61.22°, and 90°, respectively. On the other hand, the XRD pattern of the top surface of the same sample, Figure 8c, is dominated by the peaks with small interplanar angles. The high-intensity peaks of the top surface include (1 0 10), (1 0 4), (0 1 8), and (0 0 12) and have small interplanar angles of 17.5º, 38.25º, 21.51º, and 0º, respectively. To summarize the findings mentioned above, the XRD patterns of the side cross-section and the top surface are dominated by the peaks with large and small interplanar angles, respectively. In other words, the XRD patterns of the side cross-section and the top surface are complementary to each other. Consequently, these complementary lattice orientations observed between the top surface and the side cross-section show that the crystallographic texture has been successfully achieved.

3.3.2 Texture evolution during sintering

To track the texture evolution during sintering (i.e., the growth of the aligned templates), XRD characterization was conducted on the top surface of the sample with 50 wt.% nanoplatelets before and after sintering. Figure 9 shows the corresponding XRD patterns, along with the XRD pattern of the top surface of the sample without nanoplatelets, as a reference. The XRD pattern of the sample before sintering (Figure 9b) is very similar to the reference sample (Figure 9a). This similarity can be attributed to the fact that both samples have a large number of randomly orientated nanoparticles. A closer examination reveals that the intensities of the peaks with small

and large interplanar angles in Figure 9b are slightly higher and lower than those in Figure 9a, respectively. This means that adding the nanoplatelets slightly changed the XRD pattern. But after sintering, the XRD pattern (Figure 9c) is significantly changed and is dominated by the peaks with smaller interplanar angles, resulting in textured grains after TGG.

To quantify the degree of texture before and after sintering, the Lotgering factor (*LF*) was calculated based on the XRD patterns following this equation:

$$LF = \frac{p - p_0}{1 - p_0} \qquad (2)$$

where p is the sum of the intensities of the peaks for the preferred lattice orientations over the sum of the intensities of all peaks for the sample of interest (textured sample) while p_0 is the same ratio for the reference sample (untextured sample). Based on this definition, the Lotgering factor is a number between 0 and 1, where a value of 1 indicates a perfect orientation of grains [2].

Although nanoplatelets are expected to grow parallel to the basal crystal plane (0 0 6), studies have shown that they can grow with slight tilts to the basal crystal plane. Accordingly, Honda et al. used (1 1 6), (0 1 8), (1 0 10), and (1 1 9) in addition to the basal crystal plane (0 0 6) to calculate the Lotgering factor [25]. Likewise, in this study, the planes with small interplanar angles (<40°), e.g., (1 0 4), (0 0 6), (0 1 8), (1 0 10), (0 2 10), and (0 0 12), were used as the preferred lattice orientations to calculate the Lotgering factor.

Based on the data in Figure 9, the calculated Lotgering factor, i.e., the degree of texture, increased from 0.21 to 0.82 as a result of sintering. This means that a degree of texture of 0.21 was achieved through aligning the templates in the green samples and the degree of texture was increased to 0.82 through epitaxially growing the aligned templates. Thus, in the sintered samples, prepared through press-compaction-assisted binder jetting, the textured structure was primarily developed during the sintering, i.e, the grain growth of nanoplatelets at the expense of consuming nanoparticles.

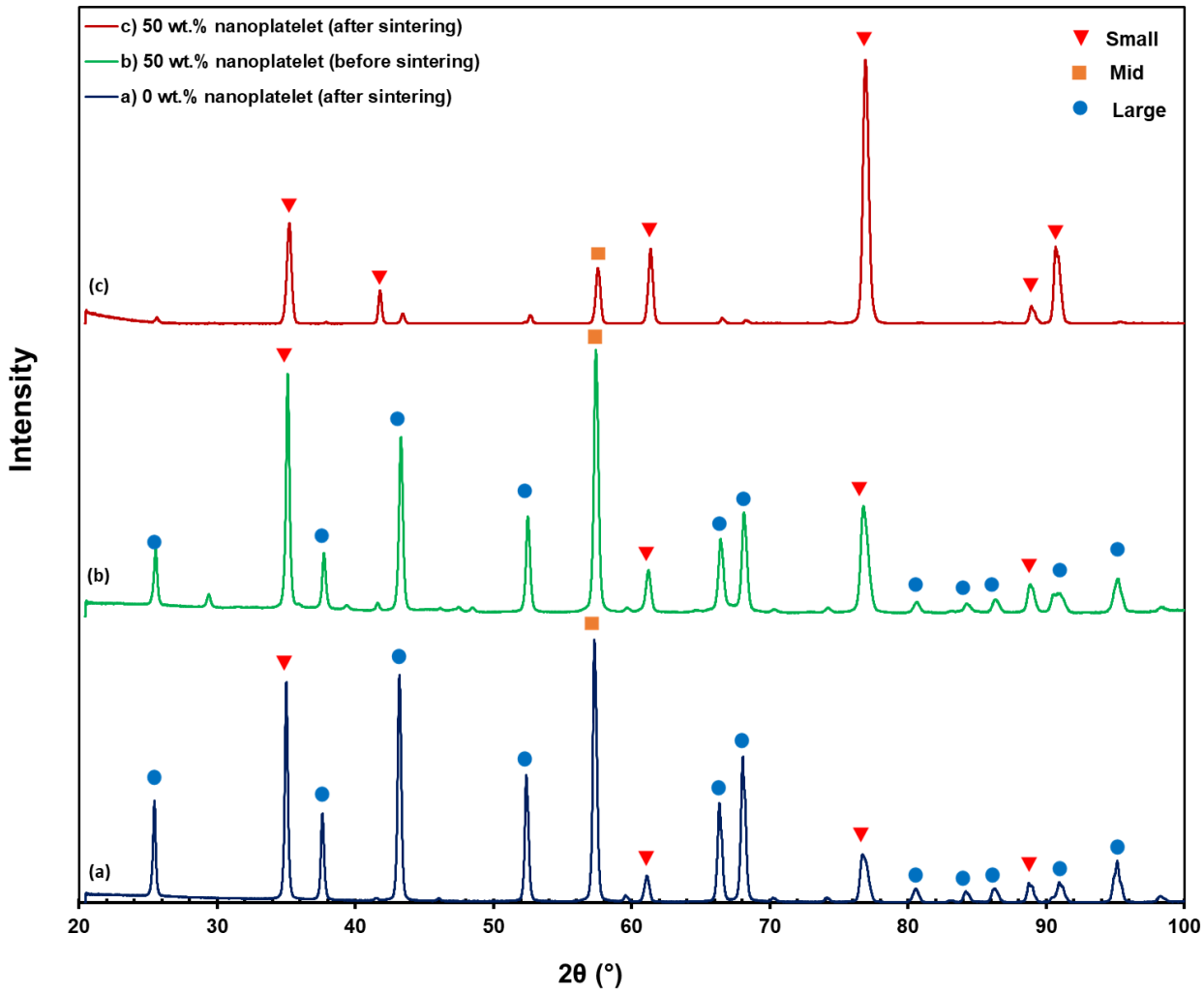

Figure 9. XRD patterns of the top surfaces of a) the sample without nanoplatelets after sintering, b) the sample with 50 wt.% nanoplatelets before sintering, and the sample with 50 wt.% nanoplatelets after sintering.

3.3.3 Effect of nanoplatelet fraction on degree of texture

XRD characterization was carried out on the sintered samples to evaluate how the nanoplatelet fraction may affect the textured structure. Figure 10 shows the XRD results obtained on the top surface of the sintered samples with various nanoplatelet fractions, from 0 wt.% to 50 wt.%. In the reference sample without nanoplatelets, different planes with a wide range of interplanar angles were diffracted. By increasing the nanoplatelet fraction, the intensities of the planes with small interplanar angles increased, while the intensities of the planes with large interplanar angles decreased. In the sample with the largest nanoplatelet fraction, all high-intensity

planes have a small interplanar angle, and the planes with a large interplanar angle have significantly diminished or disappeared.

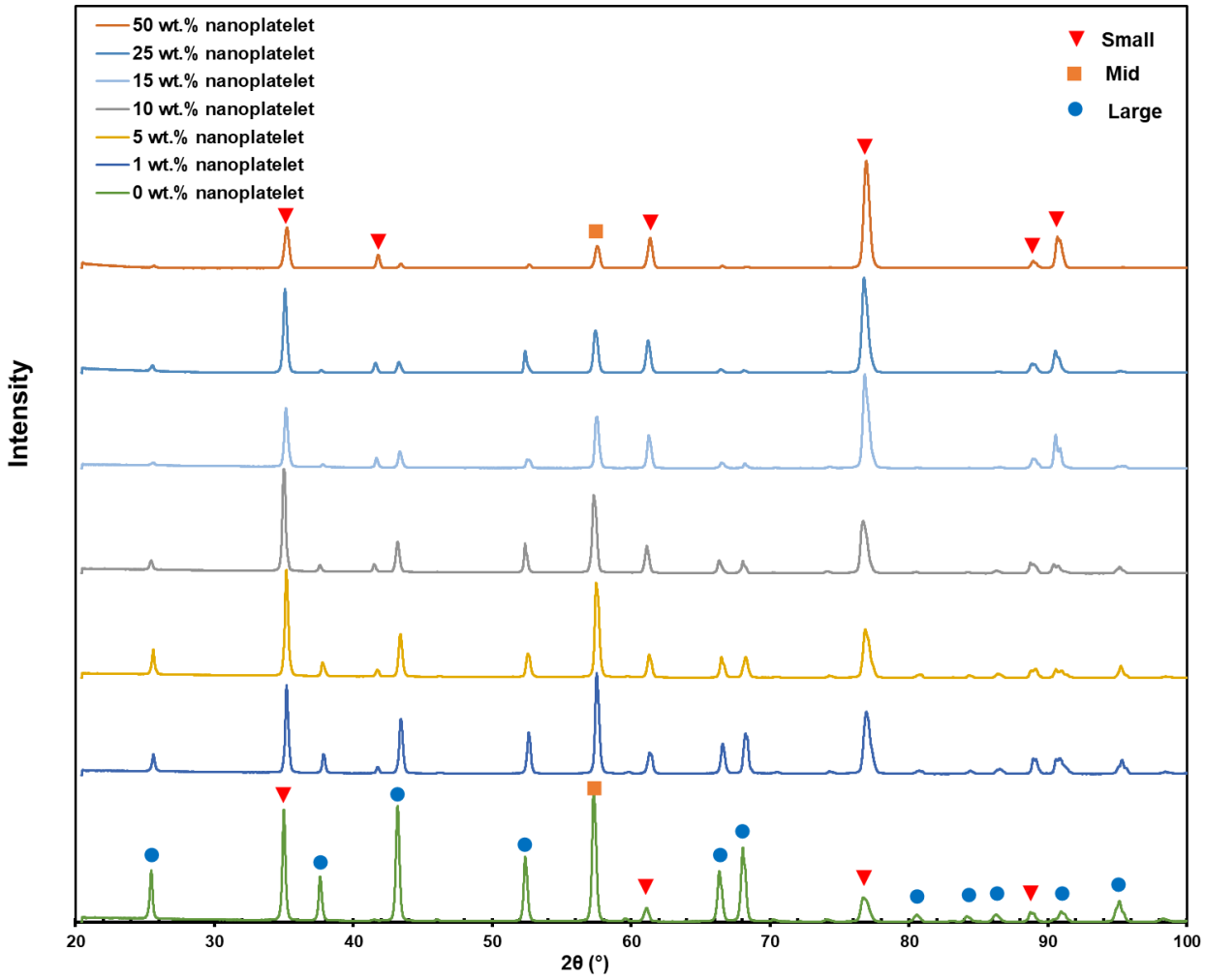

Figure 10. XRD patterns from the top surfaces of the sintered samples with various nanoplatelet fractions of 0 wt.%, 1 wt.%, 5 wt.%, 10 wt.%, 15 wt.%, 25 wt.%, and 50 wt.%.

The Lotgering factor was calculated for the samples with various nanoplatelet fractions based on the data in Figure 10. Figure 11 illustrates the Lotgering factors as a function of the nanoplate fraction. The results in Figure 11 show that as the nanoplatelet fraction increases, the Lotgering factor and the degree of texture increase. Excluding the sintered sample without nanoplatelets, the lowest and highest calculated Lotgering factors are 0.20 and 0.82 for the sintered samples with the lowest and highest nanoplatelet fractions, i.e., 1 wt.% and 50 wt.%, respectively.

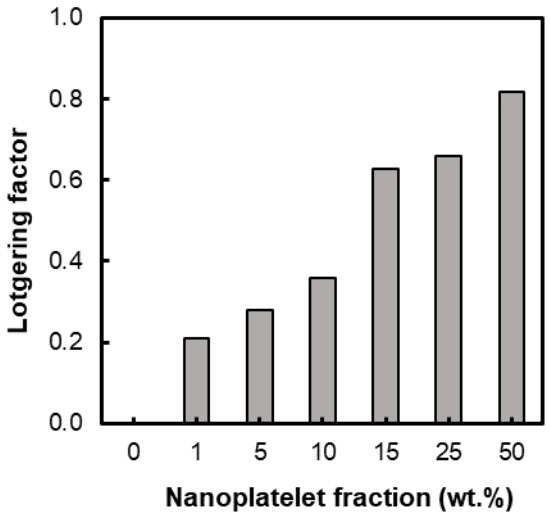

Figure 11. Calculated Lotgering factor (degree of texture) as a function of nanoplatelet fraction.

3.4 Biaxial flexural strength

Biaxial flexure tests were conducted on the samples with different nanoplatelet fractions of 0 wt.%, 5 wt.%, and 10 wt.%. Data were analyzed in the framework of Weibull statistics [26,27]. The distributions of the strength results for the three samples are plotted in Figure 12. The characteristic strength, σ_0, and Weibull modulus, m, were evaluated according to the ASTM standard [28]. The 90% confidence intervals were calculated using the maximum likelihood method. For the samples without nanoplatelets, the characteristic strength and Weibull modulus were σ_0 = 83 [56 – 125] MPa and m = 1.4 [0.9 – 2.2]. However, by adding 5 wt.% and 10 wt.% nanoplatelets, the characteristic strength increased to σ_0 = 147 [132 – 164] MPa and σ_0 = 200 [179 – 224] MPa, respectively, and the Weibull modulus increased to m = 5.2 [3.3 – 8.1] and m = 5.0 [3.2 – 7.8], respectively. The addition of the nanoplatelets influences the strength in two contrasting ways: 1) enhancing the strength through structural texturing and 2) deteriorating the strength by reducing sintered density. The results above indicate that adding nanoplatelets improved the characteristic strength and Weibull modulus of the samples under experimental conditions of this study. Thus, the effect of the textured structure on the strength was stronger than that of the reduced density. However, it is worth mentioning that while the strength of the additively manufactured samples was improved by texturing, the strength achieved in this study was lower than that achieved through conventional manufacturing processes such as tape casting [2], primarily due to the lower sintered density.

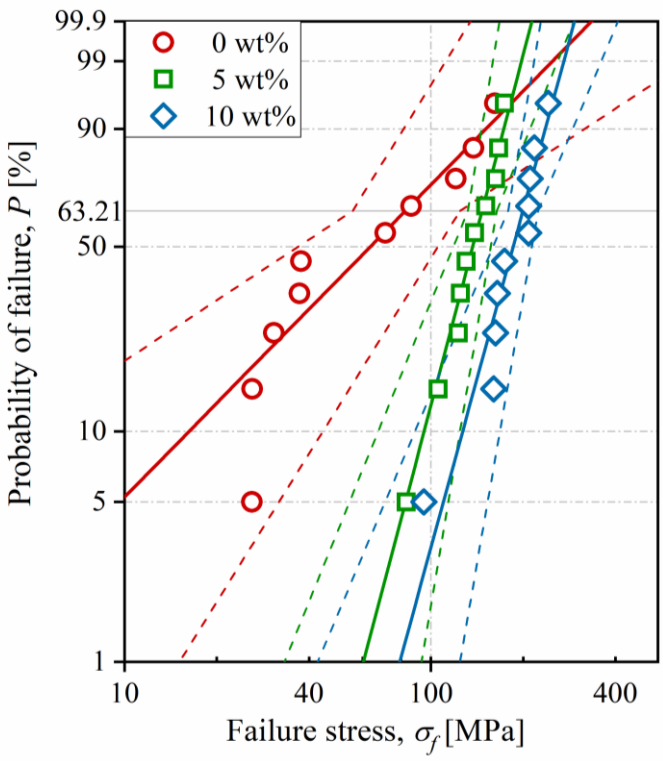

Figure 12. Probability of failure versus failure stress for the sintered samples with 0 wt.%, 5 wt.%, and 10 wt.% nanoplatelets, respectively.

4 Conclusions

This study demonstrates the successful fabrication of textured ceramics using press-compaction-assisted binder jetting. Textured alumina samples were fabricated through templated grain growth during sintering, before which nanoplatelets were aligned through press-compaction-assisted binder jetting in the green state. Various nanoplatelet fractions (up to 50 wt.%) were investigated. The increase in the nanoplatelet fraction from 1 wt.% to 50 wt.% resulted in a decrease of the sintered density from 90.4 % to 76.6 %. However, the degree of texture increased from 0.20 to 0.82. Additionally, tracking texture evolution before and after sintering indicated that the development of texture occurred mostly as a result of the growth of the preferentially aligned nanoplatelets during sintering. The Weibull analysis of the biaxial flexural tests showed that the sintered samples with 5 wt.% and 10 wt.% of nanoplatelets exhibited higher characteristic strength values, σ_0 = 147 MPa and σ_0 = 200 MPa than the samples without nanoplatelets, σ_0 = 83 MPa. These results imply the stronger effect of the increased degree of texture on the mechanical response than the reduced sintered density.

This study has effectively showcased the feasibility of producing textured ceramics through press-compaction-assisted binder jetting. However, the effects of crucial parameters on microstructure and mechanical properties remain to be explored more systematically. Such factors encompass the raw materials (e.g., templates with different fractions and distinct lattice orientations) and process parameters (e.g., layer thickness, spreading speeds, and compaction thickness). These aspects are future research directions.

Data availability

The raw data and the processed data required to reproduce these findings are available upon request from the corresponding author.

Acknowledgement

This material is based upon work partially supported by the National Science Foundation under Grant No. 2047908. A.-K. Hofer and R. Bermejo acknowledge financial support for this research provided by the European Research Council (ERC) excellent science grant "CERATEXT" through the Horizon 2020 program under Contract 817615.

Appendix

Table A1. Main diffracted planes (h k l) of α-alumina and their corresponding interplanar angles ($\emptyset_{hkl}$) with respect to the basal crystal plane (0 0 6) in a hexagonal unit cell of α-alumina [24].

(h k l)	$\emptyset_{hkl}$ (deg)	$\emptyset_{hkl}$
(0 0 6)	0	Small
(0 0 12)	0	Small
(1 0 10)	17.50	Small
(0 1 8)	21.51	Small
(1 1 9)	31.25	Small
(2 1 0)	32.23	Small
(1 0 4)	38.25	Small
(2 0 8)	38.25	Small
(1 1 6)	42.31	Medium
(1 2 8)	46.20	Medium
(0 1 2)	57.61	Large
(0 2 4)	57.61	Large
(3 0 6)	57.61	Large
(1 2 5)	59.06	Large
(1 1 3)	61.22	Large

(2 2 6)	61.22	Large
(1 2 4)	64.38	Large
(1 3 4)	70.61	Large
(2 0 2)	72.40	Large
(2 2 3)	74.64	Large
(1 2 2)	76.52	Large
(3 1 2)	80.02	Large
(4 0 2)	80.99	Large
(2 1 1)	83.16	Large
(3 1 1)	84.97	Large
(1 1 0)	90.00	Large
(0 3 0)	90.00	Large
(2 2 0)	90.00	Large

Declaration of generative AI and AI-assisted technologies in the writing process

During the preparation of this work, the authors used ChatGPT in order to improve the readability. After using this tool/service, the authors reviewed and edited the content as needed and take full responsibility for the content of the publication.

References

[1] W. Callister, D. Rethwisch, Fundamentals of materials science and engineering, 2000.

[2] Z. Zhang, X. Duan, B. Qiu, Z. Yang, D. Cai, P. He, D. Jia, Y. Zhou, Preparation and anisotropic properties of textured structural ceramics: A review, J. Adv. Ceram. 8 (2019) 289–332. https://doi.org/10.1007/s40145-019-0325-5.

[3] G.L. Messing, S. Poterala, Y. Chang, T. Frueh, E.R. Kupp, B.H. Watson, R.L. Walton, M.J. Brova, A.K. Hofer, R. Bermejo, R.J. Meyer, Texture-engineered ceramics - Property enhancements through crystallographic tailoring, J. Mater. Res. 32 (2017) 3219–3241. https://doi.org/10.1557/jmr.2017.207.

[4] X. Zhu, T.S. Suzuki, T. Uchikoshi, T. Nishimura, Y. Sakka, Texture development in Si_3N_4 ceramics by magnetic field alignment during slip casting, J. Ceram. Soc. Japan. 114 (2006) 979–987. https://doi.org/10.2109/jcersj.114.979.

[5] F. Lee, K.J. Bowman, Texture and anisotropy in silicon nitride, J. Am. Ceram. Soc. 75 (1992) 1748–1755. https://doi.org/10.1111/J.1151-2916.1992.TB07192.X.

[6] W. Kim, Y.W. Kim, D.H. Cho, Texture and fracture toughness anisotropy in silicon carbide, J. Am. Ceram. Soc. 81 (1998) 1669–1672. https://doi.org/10.1111/J.1151-2916.1998.TB02530.X.

[7] S. Li, C. Wu, K. Sassa, S. Asai, The control of crystal orientation in ceramics by imposition of a high magnetic field, Mater. Sci. Eng. A. 422 (2006) 227–231. https://doi.org/10.1016/J.MSEA.2006.02.004.

[8] K. Takatori, H. Kadoura, H. Matsuo, S. Arakawa, T. Tani, Microstructural evolution of high purity alumina ceramics prepared by a templated grain growth method, J. Ceram. Soc. Japan. 124 (2016) 432–441. https://doi.org/10.2109/jcersj2.15261.

[9] R.J. Pavlacka, G.L. Messing, Processing and mechanical response of highly textured Al_2O_3, J. Eur. Ceram. Soc. 30 (2010) 2917–2925. https://doi.org/10.1016/j.jeurceramsoc.2010.02.009.

[10] R.L. Walton, M.D. Vaudin, A.K. Hofer, E.R. Kupp, R.J. Meyer, G.L. Messing, Tailoring particle alignment and grain orientation during tape casting and templated grain growth, J. Am. Ceram. Soc. 102 (2019) 2405–2414. https://doi.org/10.1111/JACE.16144.

[11] A.K. Hofer, I. Kraleva, R. Bermejo, Additive manufacturing of highly textured alumina ceramics, Open Ceram. 5 (2021) 100085. https://doi.org/10.1016/j.oceram.2021.100085.

[12] R.L. Walton, E.R. Kupp, G.L. Messing, Additive manufacturing of textured ceramics: A review, J. Mater. Res. 36 (2021) 3591–3606. https://doi.org/10.1557/s43578-021-00283-6.

[13] R.L. Walton, M.J. Brova, B.H. Watson, E.R. Kupp, M.A. Fanton, R.J. Meyer, G.L. Messing, Direct writing of textured ceramics using anisotropic nozzles, J. Eur. Ceram. Soc. 41 (2021) 1945–1953. https://doi.org/10.1016/j.jeurceramsoc.2020.10.021.

[14] M. Moghadasi, W. Du, M. Li, Z. Pei, C. Ma, Ceramic binder jetting additive manufacturing: Effects of particle size on feedstock powder and final part properties, Ceram. Int. 46 (2020) 16966–16972. https://doi.org/10.1016/j.ceramint.2020.03.280.

[15] M. Moghadasi, G. Miao, M. Li, Z. Pei, C. Ma, Combining powder bed compaction and nanopowders to improve density in ceramic binder jetting additive manufacturing, Ceram. Int. 47 (2021) 35348–35355. https://doi.org/10.1016/J.CERAMINT.2021.09.077.

[16] W. Du, X. Ren, Z. Pei, C. Ma, Ceramic binder jetting additive manufacturing: A literature review on density, J. Manuf. Sci. Eng. 142 (2020) 1–66. https://doi.org/10.1115/1.4046248.

[17] G. Miao, W. Du, M. Moghadasi, Z. Pei, C. Ma, Ceramic binder jetting additive manufacturing: Effects of granulation on properties of feedstock powder and printed and sintered parts, Addit. Manuf. 36 (2020) 101542. https://doi.org/10.1016/j.addma.2020.101542.

[18] M. Li, G. Miao, M. Moghadasi, Z. Pei, C. Ma, Ceramic binder jetting additive manufacturing: relationships among powder properties, feed region density, and powder bed density, Ceram. Int. (2021). https://doi.org/10.1016/j.ceramint.2021.05.175.

[19] ASTM, Standard test method for apparent density of non-free-flowing metal powders using the carney funnel, ASTM Int. (2013).

[20] J. Balistreri, J. Linder, K.A. Linder, G. Pugh, W. Bircher, US patent for three- dimensional (3D) printing patent (Patent # US10449692B2), (2019).

[21] ISO, Fine ceramics (advanced ceramics, advanced technical ceramics)-determination of density and apparent porosity, ISO 18754. (2003).

[22] ASTM, Standard test method for biaxial flexure strength (modulus of rupture) of ceramic substrates, ASTM Int. (1996).

[23] M.M. Seabaugh, I.H. Kerscht, G.L. Messing, Texture development by templated grain growth in liquid-phase-sintered α-alumina, J. Am. Ceram. Soc. 80 (1997) 1181–1188. https://doi.org/10.1111/j.1151-2916.1997.tb02961.x.

[24] T. Uchikoshi, T.S. Suzuki, H. Okuyama, Y. Sakka, Fabrication of textured alumina by electrophoretic deposition in a strong magnetic field, J. Mater. Sci. 39 (2004) 861–865. https://doi.org/10.1023/B:JMSC.0000012915.76707.CA.

[25] S. Honda, S. Hashimoto, S. Iwata, Y. Iwamoto, Anisotropic properties of highly textured porous alumina formed from platelets, Ceram. Int. 42 (2016) 1453–1458. https://doi.org/10.1016/j.ceramint.2015.09.090.

[26] W. Weibull, K.T. Högskolan, A statistical theory of the strength of materials, Fifteenthfirst Ed., Gen. Litografiska Anstalts Forl. (1939). http://www.worldcat.org/title/30416455.

[27] W. Weibull, A statistical distribution function of wide applicability, J. Appl. Mech. 18 (1951) 293–297. https://doi.org/10.1115/1.4010337.

[28] ASTM, Standard practice for reporting uniaxial strength data and estimating Weibull distribution parameters for advanced ceramics, ASTM Int. (2000) 1–17.